# Structural evolution of NiAg heterogeneous alloys upon annealing

# Structural evolution of NiAg heterogeneous alloys upon annealing

O Proux†, J Mimault†, C Revenant-Brizard‡, J R Regnard†§ and B Mevel‡

† Laboratoire de Métallurgie Physique, URA CNRS 131, SP2MI, Boulevard 3, Téléport 2,
BP 179, F-86960 Futuroscope Cédex, France
‡ Département de Recherche Fondamentale sur la Matière Condensée/SP2M‖, CEA/Grenoble,
17 rue des Martyrs, F-38054 Grenoble Cédex 9, France
§ Université Joseph Fourier, BP 53 X, F-38041 Grenoble Cédex, France

**Abstract.** NiAg heterogeneous alloys were studied by x-ray diffraction and x-ray absorption spectroscopy at the Ni K-edge using a total electron yield detection. In the as-deposited $Ni_xAg_{1-x}$ alloys of 0.10 and 0.15 Ni atomic fraction, most of the Ni atoms are in substitutional sites in the Ag matrix. At higher Ni concentration, the Ni atoms outside the Ag-rich phase become numerous enough to group together in small clusters. An important disorder in the neighbourhood of Ni atoms is demonstrated. At low annealing temperature (up to 250 °C), in $Ni_{0.20}Ag_{0.80}$ and $Ni_{0.35}Ag_{0.65}$, some Ni atoms are still present in substitutional sites in the Ag matrix and the small Ni particles are under strain. A very short-range order exists in this state. After a 250 °C annealing, the Ni particles grow, and the Ag-rich phase remains in a steady structural state. After a higher annealing (400 °C), the local Ni atomic environment becomes well ordered and typical of the pure Ni FCC phase. The Ag-rich crystallites are impoverished in Ni atoms and grow with elimination of defects. Ni grains are generally smaller than 1 nm for as-deposited alloys and reach several nanometres after a 400 °C annealing for 10 min.

## 1. Introduction

The observation of giant magnetoresistance (GMR) in magnetic multilayers has stimulated considerable work on magnetic multilayers [1]. The interest in magnetic thin films was heightened by the recent discovery of GMR in heterogeneous magnetic alloys [2, 3]. These systems stimulate great interest since they have prominent merit as regards potential commercial application. Their magnetoresistance amplitudes may be larger than in multilayers in the usual current-in-plane geometry. They are also easier to prepare than multilayers and have good thermal stability after annealing. The GMR behaviour of such films has been demonstrated to be closely related to structural features. Heterogeneous alloys may be obtained by mechanical alloying [4], low-energy cluster beam deposition [5], molecular beam epitaxy [6] or more usually by co-deposition of two immiscible metals on a substrate: one is a magnetic transition metal, here Ni, and the other one is a noble metal, here Ag. According to the substrate temperature during the deposition or subsequent annealing temperatures, the formation of small magnetic domains embedded in a non-magnetic matrix may be favoured. The Ni concentrations in the Ag matrix are chosen in order to obtain medium-size particles corresponding to the optimal expected GMR. Previous structural and magnetic

‖ Laboratory associated with the Université Joseph Fourier de Grenoble (France).

characterizations indicate that the magnetic precipitates become more compact and larger after annealings [7–11]. Two contributions to the GMR are identified: the first one is linked to the transition of the magnetic grain magnetization from disordered without a magnetic field to ordered under a saturation field. The other one is the scattering of the conduction electrons by all the paramagnetic or superparamagnetic fluctuations in the material (the so-called spin-disorder scattering). The first contribution is associated with the ferromagnetic particles whereas the second one is associated with the very small magnetic particles or the magnetic atoms dispersed in the non-magnetic matrix. In the as-deposited alloys, the spin-disorder contribution is assumed to be preponderant (fine mixing of both magnetic and non-magnetic elements). One proposes that during annealing, the gradual coalescence of the magnetic element in particles increasing in size leads to the disappearance of the spin-disorder contribution in favour of the GMR contribution [12]. In that context, it appears very important to study the evolution of the nanostructure of these alloys, particularly the local atomic environment of the magnetic atoms, as a function of thermal annealings [13]. These alloys are denoted in the following $Ni_xAg_{1-x}$ with $x$ the atomic composition. The aim of the present study is first to analyse the structure of the as-deposited $Ni_xAg_{1-x}$ heterogeneous alloys versus $x$ ($x = 0.10$, 0.15, 0.20 and 0.35). Secondly, we will focus on the $Ni_xAg_{1-x}$ alloys with $x = 0.20$ and 0.35 corresponding to the concentration range where the maximum amplitude of GMR is observed for $Ni_xAg_{1-x}$ and $Co_xAg_{1-x}$. The annealing temperatures are 50, 100, 150, 250 and 400 °C. The maximum amplitude of GMR is observed after 10 min of annealing around 340 °C. The heterogeneous alloys were studied by x-ray diffraction (XRD) with Cu K$\alpha$ radiation and by conversion electron yield (CEY) x-ray absorption spectroscopy (XAS) under an He-flow atmosphere at the Ni K-edge at the French LURE-DCI synchrotron.

## 2. Experiment

### 2.1. Samples

Samples were prepared by DC magnetron sputtering of Ni and Ag on a glass substrate. The base pressure was $3 \times 10^{-8}$ mbar and the Ar pressure during the deposition was $3 \times 10^{-3}$ mbar. The relative deposition rates from both targets were adjusted to obtain the requested alloy composition. Substrates were maintained at liquid nitrogen temperature during deposition, in order to achieve a high initial degree of intermixing between the two immiscible components. The specimens were annealed in a furnace with a vacuum of $10^{-6}$ mbar at different temperatures from 50 to 400 °C for 10 min.

### 2.2. X-ray diffraction

*2.2.1. X-ray diffraction measurements and thickness considerations.* Room temperature XRD patterns were collected with a Siemens D500 powder diffractometer. $\theta$–2$\theta$ scans were recorded using Cu K$\alpha$ radiation, with a step size of 0.02° (for the 2$\theta$ angle) and a count time of 10 s. The analysis was done in the reciprocal space and figures are reported in relation to the parameter $s$ equal to $2\sin\theta/\lambda$, where $\theta$ is the angle between the incident x-ray beam and the sample surface, and $\lambda$ is the x-ray wavelength. Ni and Ag powders were used as 'standards' to correct $d$-spacing systematic errors and to estimate the instrumental broadening.

The thickness of the studied films (200 nm) was chosen to be of the same order as the sampling depth in CEY XAS measurements [14], to obtain EXAFS signals characteristic of

the whole deposited layer. This layer thickness is much less than the x-ray attenuation depth (5 $\mu$m range for Cu K$\alpha$). The Lorentz, polarization factor and absorption corrections were taken into account for the calculation. Moreover, the efficient volume is very small compared to the one used in a usual powder diffraction experiment, where the thickness is generally larger than the attenuation depth. So, in order to obtain a good signal-to-noise ratio, the time of measurement has been extended to 10 s per point.

*2.2.2. Analysis tools.* At room temperature, Ni and Ag generally crystallize in FCC structures with lattice parameters $a_{Ni} = 0.3524$ nm and $a_{Ag} = 0.4086$ nm [15]. As Ni(111) and Ag(200) peaks are located at very close angles, the reflections obtained in this reciprocal lattice area have to be examined with care. The Ag-rich phase has an intense diffracting power compared to any Ni-rich phase ($Z_{Ag} = 47$, $Z_{Ni} = 28$). So, XRD is especially sensitive to the Ag-rich phase, for which several high order reflections are obtained leading to subsequent information about composition, mean size and microstrain ratio. An Ni-rich phase has to occupy an important relative volume to be unambiguously detected, and even in this case, information will be only obtained from the (111) reflection. Some diffraction peaks are situated at slightly larger angles than the theoretical positions of the Ag(111) and Ag(222) peaks observed for pure Ag. This shows the existence of an Ag-rich FCC phase. Maximum positions of the diffraction peaks are determined by fitting with a pseudo-Voigt function, and with a standard least square reduction program [16]. As the maximum of the peaks remains close to that of pure Ag, the Vegard law can be applied with confidence to determine the Ni atomic concentration in the Ag-rich phase $C_{Ni}(Ag)$. We also define $F_{Ni}(Ag)$ as the ratio of Ni atoms included in the Ag-rich phase versus the total number of Ni atoms deposited in the films.

The whole set of specimens here studied is revealed to be highly textured. For a high fraction of crystallites, (111) dense planes are parallel to the surface of the substrate. Then, the (111) peak is always well defined and is preferentially chosen to evaluate the lattice parameter. The accuracy on the composition of the phase can be estimated taking account of two factors. The first one is the uncertainty about the peak position and the second one is the effect of stress, which has not been investigated here. For the Ag-rich phase, the uncertainty on the peak position is estimated to be $10^{-3}$ nm$^{-1}$, and leads to an uncertainty on the concentration $\Delta C_{position} = 0.5\%$ with the Vegard law assumption. Stresses in thin Ni$_x$Ag$_{1-x}$ films have already been studied [17], and the uncertainty induced by this phenomenon was estimated to be 2.5%. Hence, the absolute uncertainty is $\Delta C \sim 3\%$ for the Ag-rich phase.

The profiles of XRD peaks were analysed using the Warren–Averbach method [18] in order to separate the effects of mean size $L_W$, due to spatially limited coherently diffracting domains, from those yielded by microstrains. This analysis has to be done using two reflections of the same plane family, here, (111) and (222). The profile of these peaks is decomposed in Fourier series. The comparison of the Fourier coefficients for both peaks allows the estimation of the correlation function $V(d)$ and the microstrain ratio $\varepsilon(d)$ with $d$ the correlation vector [18]. $L_W$ is the coherence length associated with the $V(d)$ function. The calculation leads to an uncertainty of 0.5 nm on $L_W$, and of 1‰ on the microstrain ratio $\varepsilon(d)$. The $\varepsilon(d)$ parameter is revealed as a monotonically decreasing function of the correlation vector. $\varepsilon(0)$, indicated in the tables, is the upper limit and is significant of local disorder.

Such a sophisticated analysis is not applicable to the Ni-rich phase. In such a case, an estimate of the diffracting domain size $L_S$ might be obtained by the application of the Scherrer formula. It gives an overvaluation of the mean diffracting domain size, due to the presence of important microstrains not considered in this model.

## 2.3. X-ray absorption structure

*2.3.1. X-ray absorption structure measurements and analysis.* The XAS measurements were performed at LURE using synchrotron radiation from the DCI storage ring operating with an energy of 1.85 GeV. The XAS spectra were recorded at the Ni K-edge using a (331) Si channel-cut monochromator. The CEY measurements were carried out with an especially designed device cooled at liquid nitrogen temperature [19]. In this way, a good signal-to-noise ratio is obtained in an enlarged energy range, due to the reduction of the dynamic part of the Debye–Waller (DW) factor. Consequently, one can obtain accurate coordination numbers and distances.

The XANES region is used qualitatively as a 'fingerprint' of the crystallographic structure by comparing the features with those of bulk Ag or Ni.

The XAS spectra were recorded from 200 eV before the K-edge to 700 eV above. They were analysed using the same standard procedure. The edge energy was determined at the first inflexion point in the edge region. The base lines were fitted with polynomials, a first-order one before the edge and two three-order ones after the edge. The EXAFS data were Fourier transformed using a Gaussian window from 40 to 650 eV and a $k^3$-weighting. The values on the $x$-axis of the Fourier transform (FT) graphs are raw distances, i.e. they are not corrected by phase shifts.

The filtered EXAFS spectra corresponding to the FT region from 0.1 to 0.3 nm were fitted using the EXCURV92 spherical wave $X_\alpha$ model [20]. The uncertainty on the nearest neighbour (NN) coordination number is estimated to be 10% and the uncertainty on the absolute distance $R$ is 0.002 nm. For a relative comparison between the different alloys, the distance uncertainty is only 0.001 nm. The DW factor ($2\sigma^2$) uncertainty is about $0.1 \times 10^{-4}$ nm$^2$. The Ni–Ni theoretical file validity was checked with a CEY EXAFS spectrum of an FCC Ni metallic foil. For the contribution of each NN, three parameters should be fitted: the coordination number, the corresponding distance and the DW factor. Moreover, the energy reference should also be fitted for the spectrum. The number of independent parameters is determined by [21]

$$N_{idp} = (2/\pi)\,\Delta k \Delta R + 2 \tag{1}$$

where $\Delta k$ and $\Delta R$ are the data ranges in $k$- and $R$-space used to extract the fitted signal. In our case, $N_{idp}$ was estimated to be 10. Hence, three contributions could be determined.

*2.3.2. Estimation of the particle size.* The theoretical NN coordination number in an infinite crystal of Ni is denoted $N_C$. When the NN coordination number around Ni in the heterogeneous alloys is smaller than $N_C$, an estimation of the mean size of the Ni particles can be obtained from XAS. A particle is composed of a 'core' volume $V_C$ where Ni atoms have $N_C$ NN neighbours and a 'surface' volume $V_S$ containing Ni atoms located at a distance lower than $R$ from the particle surface. For these particular Ni atoms, the average number of NNs is denoted $N_S$ with $N_S < N_C$. Then, the global NN coordination number $N$ is given by:

$$N = N_C(1 - F_S) + N_S F_S \tag{2}$$

where $F_S$ is the surface-to-volume fraction $F_S = V_S/(V_C + V_S)$.

For spherical particles, a simple model [22] leads to:

$$\frac{N}{N_C} = 1 - \frac{3}{4}\frac{R}{R_p} \tag{3}$$

where $R_p$ is the radius of the particle. This expression enables us to obtain an evaluation of $R_p$ knowing the experimental $N$ and $R$ values. From equation (3), one can deduce

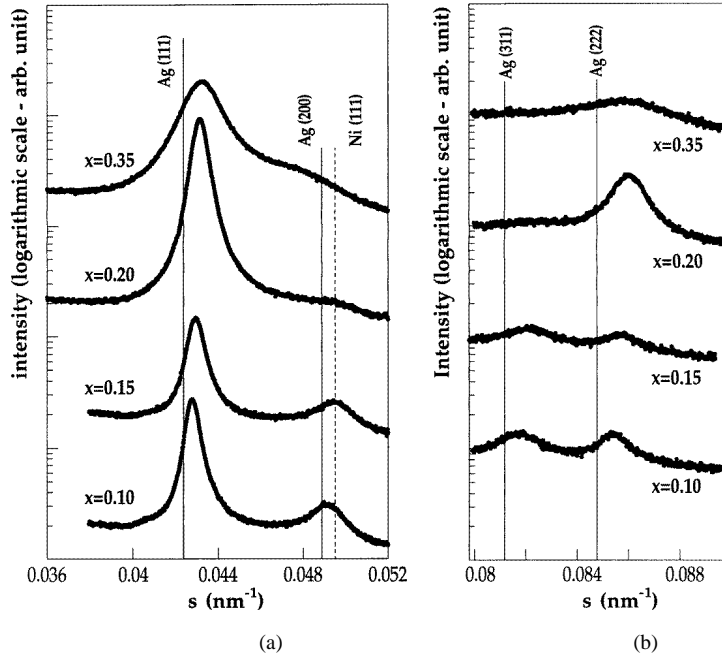$$\frac{\Delta R_p}{R_p} = \frac{\Delta(N_C - N)}{N_C - N}. \tag{4}$$

**Figure 1.** XRD patterns of the as-deposited $Ni_xAg_{1-x}$ heterogeneous alloys ($x = 0.10, 0.15, 0.20$ and 0.35) limited to the reciprocal lattice areas near and between the dense planes (111) (a) and (222) (b). The intensity is plotted with a logarithmic scale.

As $\Delta R_p$ is inversely proportional to $N_C - N$, the evaluation of $R_p$ is only revelant for small particles, typically $R_p < 2.5$ nm.

In XRD analysis, the particle size is generally estimated by the coherence length. This parameter is related to the mean thickness of the diffracting objects in the direction perpendicular to the surface for a $\theta$–$2\theta$ geometry. A spherical particle of radius $R_p$ yields a scattering similar to that of a cubic entity of same volume. Hence, one can define for spherical particles an equivalent coherence length $L_W$ of a spherical particle by $L_W \sim 1.6R_p$. For a particle studied by XRD and XAS, with an FCC lattice (lattice parameter $a$), $L_W$ can be estimated from equation (3) by:

$$L_W = 0.85a\frac{N_C}{N_C - N}. \tag{5}$$

## 3. Results

### 3.1. Nanostructure of the as-deposited $Ni_xAg_{1-x}$ alloys against x

*3.1.1. X-ray diffraction.* Figures 1(a) and 1(b) show the experimental XRD patterns in reciprocal space near the first and second order reflections of the dense planes. As the peaks are coherently located at slightly larger angles than those of Ag(111) and Ag(222) of the pure material, there is a Ag-rich FCC phase for all the probed compositions. The structural parameters of the Ag-rich phase are displayed in figure 2. $C_{Ni}(Ag)$ increases with $x$ and is always smaller than $x$. Hence, some Ni atoms are located outside the Ag-rich phase. Moreover, the ratio $F_{Ni}(Ag)$ is quite constant (about 60%) until $x = 0.20$. At large $x$, $C_{Ni}(Ag)$ tends
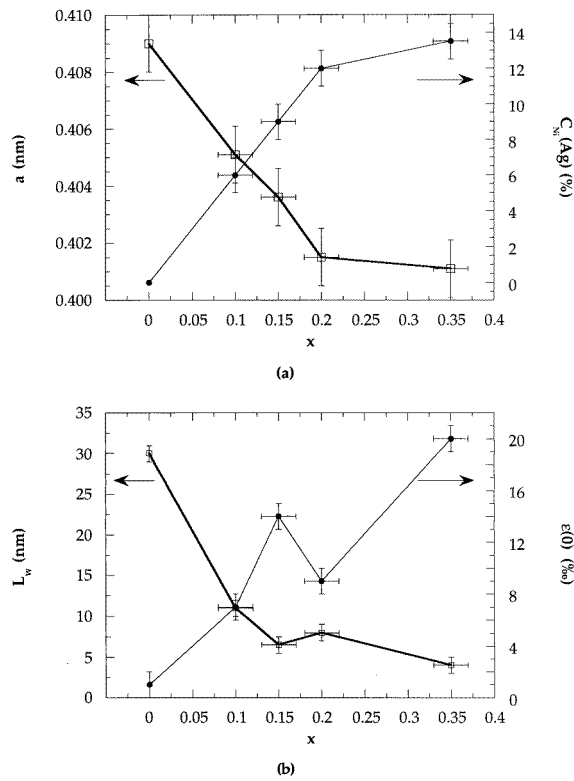
**Figure 2.** Structural parameters of the Ag-rich phase for the $Ni_x Ag_{1-x}$ as-deposited alloys from XRD. (a) Evolution of the lattice parameter $a$ (open squares) and the atomic Ni concentration in the Ag-rich phase $C_{Ni}(Ag)$ (dark circles) against $x$. (b) Evolution of the size $L_W$ (open squares) of the coherently diffracting domains and the microstrains $\varepsilon(0)$ (dark circles) against $x$.

towards a limit (about 13%). For $x = 0.35$, a large number of Ni atoms are outside the Ag-rich phase, and agglomerate. The shoulder between the Ag(111) and Ni(111) peaks can be related to this Ni-rich phase. This reflection has to be distinguished from the (200) one of the Ag-rich phase, which would be located at larger angles than the Ag(200) peak in reciprocal space.

The size $L_W$ of the Ag-rich diffracting domains globally decreases as $x$ increases. In general, size and microstrain ratio are roughly related by a decreasing monotonic function $L_W = f[\varepsilon(0)]$.

The relative intensity of the (111) reflection of the Ag-rich phase with regard to the high order reflections is much greater than that of the pure powder elements [15]. The dense planes {111} of the Ag grain are preferentially parallel to the surface for all the studied compositions. This texture is well marked for the higher Ni concentrations ($x = 0.20$ and $0.35$), where the Ag(200), and Ag(311) reflections have almost disappeared. For the $Ni_{0.20}Ag_{0.80}$ alloy, the (111) reflection of the Ag-rich phase is strongly enhanced with respect to those for less concentrated alloys. For the $Ni_{0.35}Ag_{0.65}$ alloy, the (111) reflection intensity of the Ag-rich phase is reduced compared to the $Ni_{0.20}Ag_{0.80}$ alloy. This can be explained by a lower texture degree shown by complementary measurements. This reduction can also be attributed to the combined effect of the decrease of $L_W$ and the increase of the microstrain ratio partially destroying the constructive diffraction phenomenon. The decrease of the coherence length
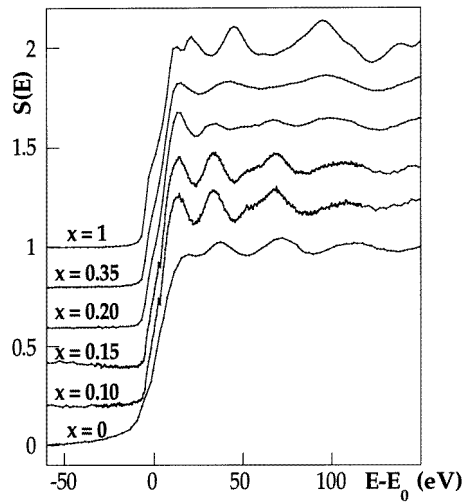
**Figure 3.** XANES spectra at the Ni K-edge of the as-deposited $Ni_xAg_{1-x}$ heterogeneous alloys ($x = 0.10, 0.15, 0.20$ and $0.35$) compared with those of bulk Ni ($x = 1$) and Ag ($x = 0$) at the Ag K-edge.
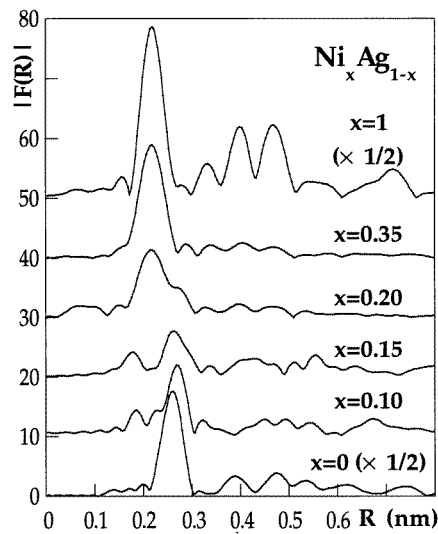


**Figure 4.** FT of the EXAFS signal of the as-deposited $Ni_xAg_{1-x}$ heterogeneous alloys ($x = 0.10$, $0.15, 0.20$ and $0.35$) compared with those of bulk Ni ($x = 1$) and Ag ($x = 0$).

together with an increase of the texture obtained when $x$ increases has to be corroborated by complementary experiments.

*3.1.2. X-ray absorption spectroscopy.* The XANES spectra of the as-deposited alloys (figure 3) differ substantially from that of bulk Ni. For $x = 0.10$ and $0.15$, they appear rather similar to that of bulk Ag. For these alloys, an important fraction of Ni atoms is located in substitutional sites in the FCC Ag matrix and form a dilute phase. As $x$ increases, a larger

fraction of Ni atoms is present out of this solid phase. XANES spectra of the as-deposited alloys exhibit only one peak in the first 25 eV region after $E_0$. From Montano *et al* [23] the absence of two peaks in the XANES of a microcluster with an FCC structure, in contrast with the XANES of the bulk metal, indicates the absence of fourth and higher shell atoms in the cluster.

The FTs of the as-deposited alloys (figure 4) confirm and clarify this behaviour. The FT of the $Ni_{0.10}Ag_{0.90}$ alloy exhibits only one well defined peak, typically positioned close to the NN distance in an FCC Ag matrix. As *x* increases, this peak gradually decreases and another peak, typically positioned at the NN distance in an FCC Ni matrix, increases. Moreover, the FTs of the as-deposited alloys have no marked features after 0.3 nm indicating a strong disorder around Ni.

The filtering process was performed to take into account both Ni–Ni and Ni–Ag contributions in the fitting procedure. A good coherence of this model is obtained for the whole spectrum set. In particular, the signature of a significant Ni–Ag atomic pair fraction is directly visible on the filtered EXAFS spectra, as the phase shift of the EXAFS signal reverses progressively from $x = 0$ to 1, with respect to the pure FCC Ni one, at $k = 0.4$ and $1.1$ nm$^{-1}$ (figure 5).
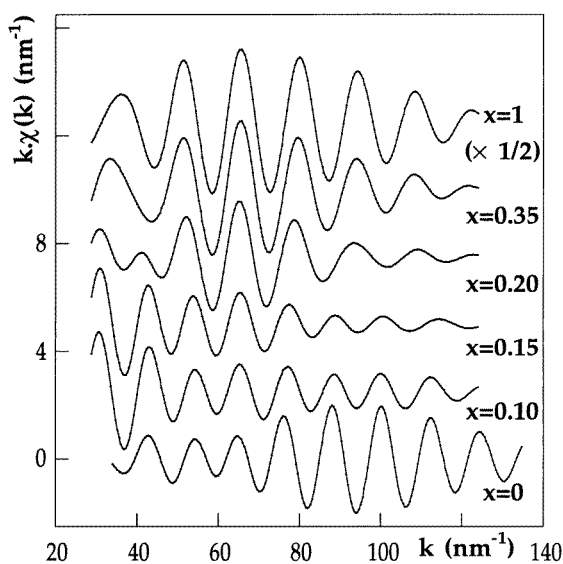


**Figure 5.** Filtered EXAFS spectra of the as-deposited $Ni_xAg_{1-x}$ heterogeneous alloys ($x = 0.10$, 0.15, 0.20 and 0.35) compared with those of bulk Ni ($x = 1$) and Ag ($x = 0$). Filtering was performed to take into account both Ni–Ni and Ni–Ag contributions. The filtering FT window was taken from 0.1 to 0.3 nm.

Among the distances indicated in table 1, those around 0.275 nm are related to the Ni–Ag pairs in the Ag-rich phase, corresponding to isolated Ni atoms (surrounded by 12 Ag neighbours). These experimental NN distances are smaller than that of the bulk Ag (0.288 nm at $-196\,°C$). The alloying phenomenon gives rise to an important local disorder. Such large DW values certainly induce a negative shift of the so-obtained distance value. A cumulant method would be more appropriate to obtain the real distance, but its application in such a complex neighbourhood is not trivial. Nevertheless, the uncertainty brought by the used analysis does not completely explain the difference from the Ag pure matrix NN distance. One can also

**Table 1.** Fit results of the filtered EXAFS spectrum of the as-deposited alloys. The parameter $N$ is the NN coordination number, $R$ the NN coordination distance (in nm), and $2\sigma^2$ the DW factor (in $10^{-4}$ nm$^2$). Filtering was performed to take into account both Ni–Ni and Ni–Ag contributions. The filtering FT window was taken from 0.1 to 0.3 nm. For comparison, pure Ni: $N = 12$, $R = 0.248$ nm, $2\sigma^2 = 0.8 \times 10^{-4}$ nm$^2$.

| | $Ni_{0.10}Ag_{0.90}$ | | | $Ni_{0.15}Ag_{0.85}$ | | | $Ni_{0.20}Ag_{0.80}$ | | | $Ni_{0.35}Ag_{0.65}$ | | |
| --- | --- | --- | --- | --- | --- | --- | --- | --- | --- | --- | --- | --- |
| | $N$ | $R$ | $2\sigma^2$ | $N$ | $R$ | $2\sigma^2$ | $N$ | $R$ | $2\sigma^2$ | $N$ | $R$ | $2\sigma^2$ |
| Ag-rich phase | | | | | | | | | | | | |
| Ni–Ag | 8.1 | 0.276 | 2.2 | 6.9 | 0.273 | 2.1 | 4.5 | 0.275 | 2.4 | 1.6 | 0.272 | 2.4 |
| Ni–Ni | 1.3 | 0.266 | 2.2 | 1.2 | 0.267 | 2.1 | — | — | — | — | — | — |
| Ni-rich phase | | | | | | | | | | | | |
| Ni–Ni | 1.2 | 0.244 | 1.2 | 1.7 | 0.244 | 1.4 | 4.7 | 0.247 | 1.4 | 6.4 | 0.247 | 1.3 |

assume an important core effect around Ni atoms, due to the substantial difference of the Ni and Ag atomic radii.

The Ni–Ni pairs (0.244 nm $< R <$ 0.247 nm) are indicative of an Ni-rich FCC phase, out of the Ag-rich one. This distance is slightly smaller than the pure bulk one (0.249 nm at $-196\,^{\circ}$C). Such distance reductions are generally encountered in small particles thinly distributed or dispersed in the deposited layer and under strain in the material [23]. For the $x = 0.20$ and $x = 0.35$ alloys, where the size of the Ni particles is larger, the Ni–Ni distance increases towards that of bulk Ni.

For $x = 0.10$ and 0.15, the contribution of some Ni–Ni bonds with a distance $R = 0.266$ nm is also needed to obtain a good fit. No argument can support the hypothesis of this bond distance in a pure nickel aggregate: it was preferred to attribute this 'intermediate' bond distance (between 0.248 and 0.275) to very small agglomerates (Ni pairs) which remained in coherence with the Ag matrix.

### 3.2. Nanostructure of the $Ni_{0.20}Ag_{0.80}$ and $Ni_{0.35}Ag_{0.65}$ versus thermal annealings

*3.2.1. X-ray diffraction.* Figures 6(a) ($x = 0.20$) and 6(b) ($x = 0.35$) display the experimental XRD patterns, limited to the reciprocal lattice area near the Ag(111) and Ni(111) reflections. Two temperatures (250 and 400 $^{\circ}$C) were selected to illustrate the structural evolution from the as-deposited state. Complementary XRD patterns were recorded around the (311) and (222) peak positions of the pure Ag FCC lattice. A high degree of texture is observed for both compositions.

The values of the deduced structural parameters reported in table 2 show that the demixing process is not occurring during the 250 $^{\circ}$C annealing, but after a 400 $^{\circ}$C annealing, leading to a weak Ni concentration (2–5%) in the Ag-rich phase. Microstrain ratio values and the mean size of the Ag grain evolves in a reverse way. These values of microstrain and coherence length still agrees with the previous function $L_W = f[\varepsilon(0)]$ noted in section 3.1.1.

From the values of $C_{Ni}(Ag)$ smaller than $x$, one can deduce the existence of an Ni-rich phase. For $x = 0.35$, the large and smooth diffraction peak related to the Ni-rich phase is shifted towards the theoretical position of the pure Ni(111) after a 250 $^{\circ}$C annealing. After a 400 $^{\circ}$C annealing, the peak position is very close to that of pure Ni. For $x = 0.20$, a very weak peak appears directly pointed at the Ni(111) position. This peak is probably related to the (111) peak of the pure Ni phase and not to the Ag(200) peak, because the Ag-rich phase is highly textured along the (111) dense planes and the Ag(200) peak is expected to follow the behaviour of the Ag(311) peak which only appears after a 400 $^{\circ}$C annealing.
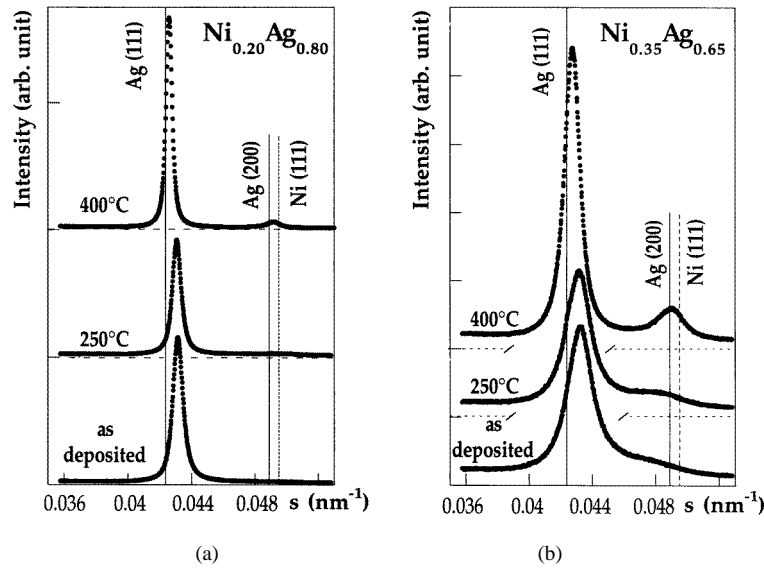
**Figure 6.** (a) XRD patterns of the $Ni_{0.20}Ag_{0.80}$ alloys as-deposited and annealed at 250, 400 °C limited to the reciprocal lattice area near the Ag(111) theoretical reflection. (b) XRD patterns of the $Ni_{0.35}Ag_{0.65}$ alloys as deposited and annealed at 250, 400 °C limited to the reciprocal lattice areas near and between the theoretical reflections Ag(111) and Ni(111).

**Table 2.** Structural parameters of the Ag-rich phase for the $Ni_{0.20}Ag_{0.80}$ and $Ni_{0.35}Ag_{0.65}$ alloys from XRD as a function of annealing. The parameter $a$ is the lattice parameter, $C_{Ni}$(Ag) the atomic Ni concentration in the Ag-rich phase, $L_W$ the size of the coherently diffracting domains and $\varepsilon(0)$ the microstrains.

|  | $Ni_{0.20}Ag_{0.80}$ | | | $Ni_{0.35}Ag_{0.65}$ | | |
|---|---|---|---|---|---|---|
|  | As dep. | 250 °C | 400 °C | As dep. | 250 °C | 400 °C |
| $a$ (nm) | 0.4015 | 0.4025 | 0.407 | 0.401 | 0.4015 | 0.406 |
| $C_{Ni}$(Ag) (%) | 12.5 | 12 | 2 | 13.5 | 13 | 5 |
| $L_W$ (nm) | 9 | 8 | 17 | 4 | 3.5 | 7.5 |
| $\varepsilon(0)$ (‰) | 9 | 10 | 5.5 | 20 | 20 | 8.5 |

*3.2.2. X-ray absorption spectroscopy.* Figures 7(a) and 7(b) display the FTs of the $Ni_{0.20}Ag_{0.80}$ and $Ni_{0.35}Ag_{0.65}$ EXAFS spectra from as-deposited to annealed up to 400 °C. Up to 250 °C, the FTs are very similar with no well pronounced features at distances larger than 0.3 nm. Hence, in this temperature range, the local Ni atomic environment is stable and characteristic of a very short-range order. Anyhow, one can notice a slight increase of the intensity of the FT peaks, for both compositions after a 250 °C annealing, on the entire distance range, reflecting the onset of a structural change. After a 400 °C annealing, the FTs for both compositions present well marked and intense features tending towards those of the bulk Ni FT. At that stage, the local environment of Ni atoms becomes well ordered.

Fit results are reported in table 3. The Ni–Ni NN distance is close to the bulk metallic Ni. Up to a 250 °C annealing and for both compositions, the DW factor $2\sigma^2_{Ni-Ni}$ is larger than the bulk Ni one, and reflects an important disorder in the neighbourhood of the Ni atoms. As the annealing temperature increases, this DW term decreases up to $0.9 \times 10^{-4}$ nm$^2$ at 400 °C and simultaneously the Ni–Ni coordination number increases towards the value of bulk Ni.
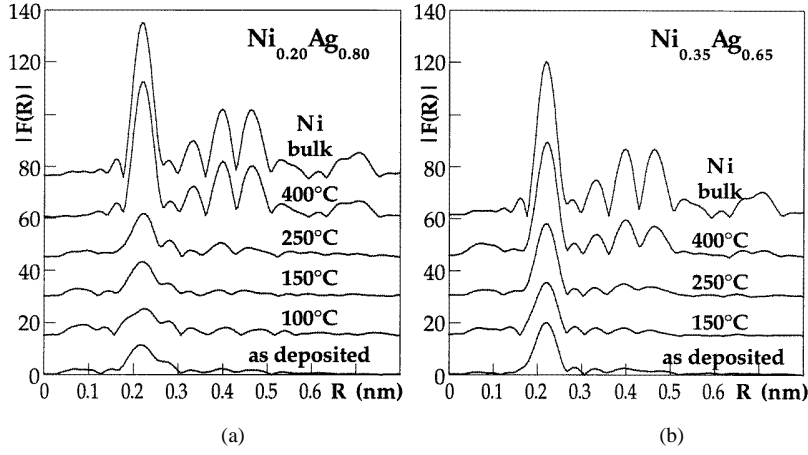
**Figure 7.** (a) FT of the EXAFS signal of the $Ni_{0.20}Ag_{0.80}$ alloys as deposited and annealed at 100, 150, 250 and 400 °C compared with the bulk Ni FT. (b) FT of the EXAFS signal of the $Ni_{0.35}Ag_{0.65}$ alloys as deposited and annealed at 150, 250 and 400 °C compared with the bulk Ni FT.

**Table 3.** Fit results of the filtered EXAFS spectrum for the $Ni_{0.20}Ag_{0.80}$ and $Ni_{0.35}Ag_{0.65}$ alloys annealed at 250 and 400 °C. The parameter $N$ is the NN coordination number, $R$ the NN coordination distance (in nm) and $2\sigma^2$ the DW factor (in $10^{-4}$ nm$^2$). Filtering was performed to take into account both Ni–Ni and Ni–Ag contributions. The filtering FT window was taken from 0.1 to 0.3 nm. For comparison, pure Ni: $N = 12$, $R = 0.248$ nm, $2\sigma^2 = 0.8 \times 10^{-4}$ nm$^2$.

| | | $Ni_{0.20}Ag_{0.80}$ | | | $Ni_{0.35}Ag_{0.65}$ | | |
| --- | --- | --- | --- | --- | --- | --- | --- |
| | | $N$ | $R$ | $2\sigma^2$ | $N$ | $R$ | $2\sigma^2$ |
| 250 °C | Ni–Ag | 3.8 | 0.279 | 1.9 | — | — | — |
| | Ni–Ni | 5.8 | 0.248 | 1.2 | 8.1 | 0.247 | 1.2 |
| 400 °C | Ni–Ni | 11.3 | 0.248 | 0.9 | 10.4 | 0.248 | 0.9 |

The Ni–Ag contribution decreases as the annealing process goes on. After a 250 °C annealing, the coordination numbers and the DW factors show only slight variations. The DW factor remains large, between twice and three times the bulk Ni one. It reflects a large disorder around the solute atoms of this metastable Ag-rich phase. For $x = 0.35$ and a 250 °C annealing, the Ni–Ag contribution in the Ag-rich phase cannot be determined accurately because its magnitude is of the order of the uncertainty. The addition of the minimum contribution ($N = 1$ with $R = 0.275$ nm and $2\sigma^2 = 2 \times 10^{-4}$ nm$^2$) is at the limit of sensitivity of the fit quality parameter.

## 4. Size estimation of the magnetic grains

Whatever the concentration and the annealing, the total NN coordination number around an Ni atom does not reach 12, as it would in a bulk FCC environment. For the Ag-rich phase, we denote by $N_C(Ag)$ the partial coordination number of Ni, which would be given in a well crystallized Ag phase disseminated in the alloy. $N_C(Ag)$ is defined as follows:

$$N_C(Ag) = N_C F_{Ni}(Ag) \text{ with } N_C = 12. \tag{6}$$

We denote by $N(\mathrm{Ag})$ the experimental NN coordination number of Ni in this particular Ag-rich phase.

$$N(\mathrm{Ag}) = [N(\mathrm{Ni-Ag}) + N(\mathrm{Ni-Ni})]. \tag{7}$$

An estimation of the lack of coordination number $[N_C(\mathrm{Ag}) - N(\mathrm{Ag})]/N_C(\mathrm{Ag})$ can be obtained from relation (5) by using the coherence length $L_W$ determined by XRD. The replacement of the $N(\mathrm{Ag})$ value found by EXAFS in this relation enables us to obtain an estimate of $N_C(\mathrm{Ag})$. It must be mentioned that $[N_C(\mathrm{Ag}) - N(\mathrm{Ag})]/N_C(\mathrm{Ag})$ remains generally weak and does not bring an important change in the final result, except the case $x = 0.35$, for which the correction reaches 9%.

As previously seen, the magnetic phase seems to be pure Ni. Consequently, considering that all the Ag atoms are included in the Ag-rich phase, the previously obtained $N_C(\mathrm{Ag})$ value allows us to deduce the Ni atomic fraction, $F_{Ni}(\mathrm{Ag})$, and the corresponding atomic composition $C_{Ni}(\mathrm{Ag})$ in the Ag-rich phase is reported in figure 8 and table 4. They have to be compared to the XRD results previously given in figure 2 and table 2. The mean values of $C_{Ni}(\mathrm{Ag})$ obtained from the x-ray and EXAFS results are used to propose an estimation of the partial coordination number $N_C(\mathrm{Ni})$, which would be given in a pure well formed Ni phase disseminated in the alloy. Then, the mean value of $N_C(\mathrm{Ni})$ is also defined as follows:
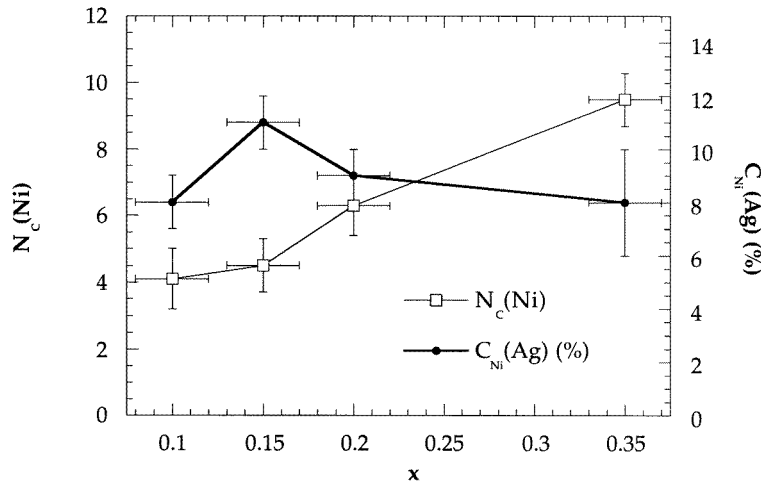
$$N_C(\mathrm{Ni}) = 12 - N_C(\mathrm{Ag}). \tag{8}$$



**Figure 8.** Evolution of $N_C(\mathrm{Ni})$ and $C_{Ni}(\mathrm{Ag})$ against $x$ for the $\mathrm{Ni}_x\mathrm{Ag}_{1-x}$ as-deposited alloys. $N_C(\mathrm{Ni})$ is the partial coordination number of Ni, which would be given by a pure well formed Ni phase disseminated in the alloy and $C_{Ni}(\mathrm{Ag})$ is the Ni atomic concentration in the Ag-rich phase. The mean value of $N_C(\mathrm{Ni})$ is the average of the values obtained by XRD and EXAFS.

$N_C(\mathrm{Ni})$ is found to be larger than the experimental $N(\mathrm{Ni})$ given by the EXAFS fits (tables 1 and 3). The radius $R_p$ is obtained from the expression (3) by using the mean value $N_C(\mathrm{Ni})$ and taking $R$ equal to 0.25 nm. For $x = 0.10$ and 0.15, this radius is estimated to be $0.30 \pm 0.03$ nm; for $x = 0.20$ and 0.35, $R_p$ values are reported in table 4. For the annealed alloys, except the case $x = 0.20$ and a 250 °C annealing, $C_{Ni}(\mathrm{Ag})$ is very weak from the EXAFS analysis. Then, in these cases, the mean value $N_C(\mathrm{Ni})$ is probably overvalued, particularly for $x = 0.35$ and a 250 °C annealing, where XRD results show a non-negligible Ni concentration in the Ag-rich phase. Then, the so-obtained $R_p$ is certainly underestimated.

**Table 4.** Estimation of the Ni grain radius for the $Ni_{0.20}Ag_{0.80}$ and $Ni_{0.35}Ag_{0.65}$ alloys as a function of annealing. The parameter $C_{Ni}(Ag)$ is the Ni atomic concentration in the Ag-rich phase, $N_C(Ni)$ the partial coordination number of Ni, which would be given by a pure well formed Ni phase disseminated in the alloy. $R_p$ is the mean radius of Ni particles. The mean value of $N_C(Ni)$ and $R_p$ is the average of the values obtained by XRD and EXAFS.

| | $Ni_{0.20}Ag_{0.80}$ | | | $Ni_{0.35}Ag_{0.65}$ | | |
|---|---|---|---|---|---|---|
| | As dep. | 250 °C | 400 °C | As dep. | 250 °C | 400 °C |
| EXAFS $C_{Ni}(Ag)$ (%) | 9 | 8 | 0 | 7 | 0 | 0 |
| Mean value $N_C(Ni)$ | 6.3 | 6.7 | 11.5 | 9.5 | 10.2 | 11.4 |
| Mean size $R_p$ (nm) | 1 | 1.4 | 9 | 0.6 | 0.9 | 2 |
| $\Delta R_p/R_p$ (%) | 45 | 20 | 40 | 20 | 10 | 10 |

## 5. Discussion

### 5.1. On the structure of the different phases

The particle size of the Ni- and Ag-rich phases is based on results presenting different degrees of confidence. The (111) diffraction peak position of the Ag-rich phase is always well defined. The Vegard law is rarely questioned for small shifts of the relevant diffraction peaks. However, this analysis is not free from errors. The XRD patterns are analysed assuming an additive contribution of two phases in total incoherence. The important disorder degree can generate some deviations. In EXAFS, the Ni–Ni contribution is fitted accurately. In the contrast, the Ni–Ag one is more difficult to estimate when $x$ increases. So, the previously stated results have to be taken as an order of magnitude rather than accurate values.

*5.1.1. As-deposited films.* For $x = 0.10$ and 0.15, both techniques, XRD and EXAFS, lead to similar values for the composition of the Ag-rich phase. More precisely, EXAFS yields a slightly larger $C_{Ni}(Ag)$ value compared to that from XRD. The analysis concludes that a very limited fraction of Ni atoms relative to the total atomic population is present in agglomerates having the Ni bulk FCC lattice. This fraction can be estimated by $x(1 - F_{Ni}(Ag))$ i.e. about 4% for $x = 0.10$ and 6% for $x = 0.15$. In such a case, it seems effectively reasonable to obtain very small pure Ni particles because, in the incident atomic flow during the sputtering process, the high percentage of Ag atoms rapidly prevents a large spatial development of pure Ni FCC particles. Moreover, the Ni–Ni distance obtained by EXAFS (0.244 nm) is smaller than that for bulk Ni. This is generally typical of very small particles. EXAFS and XRD estimations yield close radius values for Ni particles.

For $x = 0.20$ and 0.35, the Ni–Ni distance (0.247 nm) is close to that of pure FCC Ni. For these concentrations, a significant atomic fraction of the whole matrix (about 10% for $x = 0.20$ and 25% for $x = 0.35$) is composed of an Ni-rich phase constituted of well formed particles. Nevertheless, differences in the $C_{Ni}(Ag)$ values deduced from XRD and EXAFS techniques become large. For these high concentration alloys, the EXAFS technique yields a smaller $C_{Ni}(Ag)$ value compared to the XRD technique. The difference in $C_{Ni}(Ag)$ between both techniques probably comes from the difficulty of obtaining from EXAFS an accurate estimation of the Ni–Ag contribution in the Ag-rich phase. The high DW value related to this contribution makes it ineffective and yields the high-energy EXAFS signal rather typical of the complementary pure and well structured Ni phase in the film. The weight of this Ni-rich phase in the EXAFS signal becomes important (about 50% for $x = 0.20$ and 75% for $x = 0.35$).

*5.1.2. Annealed films.* For both compositions, increasing temperature favours Ni agglomeration. Except the case $x = 0.20$, and $T = 250\,°\text{C}$, the Ni–Ag contribution is very small (null within the uncertainty). Then, the calculation of $N_C(\text{Ni})$ by the EXAFS technique cannot be complete and this certainly yields some uncertainties. This is particularly true for the alloy $x = 0.35$ annealed at $T = 250\,°\text{C}$, where the XRD analysis shows a quasi-stability of the Ni concentration in the Ag-rich phase (in peak position and magnitude). From both the XRD and EXAFS results, only the Ni phase changes at this temperature.

After the $400\,°\text{C}$ annealing, the demixing of the Ag-rich phase is well advanced. Then, the values of the Ni particle radius issued from the simulations can be taken with more confidence.

### 5.2. Comments on the secondary x-ray diffraction peak

For $x = 0.35$, XRD patterns display a small and broad peak for the as-deposited and $250\,°\text{C}$ annealed alloy, between the peaks of (111) dense planes of pure Ag and Ni. This peak does not exist for the alloys with smaller $x$. The existence of this peak can be related to the large proportion of the Ni-rich phase obtained for this composition. The common analysis generally consists in modelling diffraction patterns by summing two independent peaks. The scattered intensity is, then, assumed to originate from two nanocrystalline FCC phases entangled and in complete structural incoherence. Such a simulation can be performed with diffraction profiles of pseudo-Voigt types. This interpretation yields a lattice parameter of about $0.37$ nm for the Ni-rich phase, leading to a composition of around 35% of Ag atoms by applying the Vegard law. Applying the Scherrer relation to its FWHM gives an Ni particle size around $1.5$ nm, which must be considered as a minimum, taking into account the used method. However, such composition and lattice parameter are incompatible with the local atomic environment indicated by EXAFS (atomic nature, NN distance and coordination number). A different model [24, 25] consists in questioning the total structural incoherence between the two FCC phases. Such a diffraction analysis, based on a partial coherence degree in the stacking of dense planes at the interface between pure Ni particles and the Ag-rich phase, yields results in good agreement with the EXAFS ones (NN distances, radius of pure Ni particles, and composition of the Ag-rich phase). This point will be the object of a detailed study in a further paper.

### 6. Conclusions

Heterogeneous NiAg alloys were studied by XRD and XAS at the Ni K-edge by CEY. In the as-deposited $\text{Ni}_x\text{Ag}_{1-x}$ alloys, Ni particles of nanometre size are formed and embedded in an Ag-rich phase. The Ni concentration in this Ag-rich phase is rapidly saturated. At low Ni concentration ($x = 0.10, 0.15$), small Ni particles (mean radius around $0.3$ nm) are formed and remain under high strain in the as-deposited film. The characteristic NN distance around an Ni atom in the Ag-rich phase is found to be around $0.275$ nm, a value close to that of pure FCC Ag. Whatever the composition, an important local disorder is demonstrated in the Ag-rich phase. The microstrain ratio related to the long-scale disorder is also important. It increases with the whole Ni concentration and when the size of the Ag-rich particles decreases.

At low annealing temperature (up to $250\,°\text{C}$), the diffusion appears non-existent. The local Ni atomic environment, in particular the very short-range order, appears very stable. Clustering of Ni obviously occurs after the $250\,°\text{C}$ annealing and appears particularly evident in the alloys with $x = 0.35$. For this composition, Ni clusters are growing with their mean size multiplied by a factor of about $1.5$. For both compositions ($x = 0.20$ and $0.35$), the annealing at $250\,°\text{C}$ accelerates the Ni clustering; meanwhile the structure of the Ag-rich phase appears very stable. The clustering only operates through a competitive growth of the particles already formed.

At higher annealing temperature, the demixing also contributes to the growth of the particles and the local Ni atomic environment becomes well ordered. EXAFS signals become very similar to a pure Ni one and the mean size of the Ni particle reaches several nanometres. After a 400 °C annealing, the demixing is almost finished. For $x = 0.35$, the Ag-rich phase becomes impoverished in Ni from 13.5 to 5% in 10 min. The Ag-rich crystallites grow with elimination of the defects. Microstrain ratio and mean size of particles evolve with the same relation previously noticed for as-deposited alloys.

The importance of the GMR seems to be mainly related to the distance between the magnetic clusters. A simple calculation, based on atomic ratio considerations and assuming that the clusters are equidistant, spherical and of the same size, shows that for the two samples which exhibit the maximum GMR (for $x = 0.35$ in the as-deposited and 250 °C annealed states), the distance between the nickel clusters is around 2 nm. For the other samples, for which the GMR amplitude is much smaller, this distance is strongly increased.

The analysis of the Ag K-edge XAS experiments performed by CEY at liquid nitrogen temperature at ESRF (European Synchrotron Radiation Facility) on the French CRG/IF (Collaborating Research Group/Interface) is now in progress. Moreover *in situ* XAS experiments [26] were performed in the 250–400 °C annealing range where the structural characteristics change drastically and the GMR becomes maximum.

## Acknowledgments

## References

[1] Barthelemy A, Cros V, Duvail J L, Fert A, Morel R, Parent F, Petroff F and Steren L B 1995 *Nanostruct. Mater.* **6** 217

[2] Berkowitz A, Young A P, Mitchell J R, Zang S, Carey M J, Spada F E, Parker F T, Hutten A and Thomas G 1992 *Phys. Rev. Lett.* **68** 3745

[3] Xiao G, Jiang J S and Chien C L 1992 *Phys. Rev. Lett.* **68** 3749

[4] Xu J, Herr U, Klassen T and Averback R S 1996 *J. Appl. Phys.* **79** 3935

[5] Dupuis V, Tuaillon J, Perez J P, Paillard V, Perez A, Melinon P, Thomas L, Barbara B and Bouchet B 1995 *J. Magn. Magn. Mater.* **148** 1

[6] Azizi A, Thompson S M, Ounadjela K, Gregg J, Vennegues P, Dinia A, Arabski J and Fermon C 1995 *J. Magn. Magn. Mater.* **148** 313

[7] Cowache C, Dieny B, Teixeira S R and Redon O 1994 *Proc. Int. Symp. on Magnetism in Systems of Reduced Dimension, KOUROVKA '95 (Ekaterimburg, 1994)*

[8] Regnard J R, Juanhuix J, Brizard C, Dieny B, Mevel B, Mimault J and Proux O 1996 *Solid State Commun.* **97** 419

[9] Regnard J R, Revenant-Brizard C, Dieny B, Mevel B and Mimault J 1996 *Mater. Res. Soc. Symp. Proc.* vol 400 (Pittsburgh, PA: Materials Research Society) p 329

[10] Revenant-Brizard C, Regnard J R, Mimault J, Proux O, Dieny B and Mevel B 1997 *J. Physique Coll.* IV **7** C2 1111

[11] Revenant C, Simon J P, Regnard J R, Manzini I and Rodmacq B 1998 *J. Appl. Crystallogr.* **31** 783

[12] Chamberod A, Cowache C, Dieny B, Pierre J, Redon O, Rodmacq B and Teixeira S 1995 *J. Magn. Magn. Mater.* **140** 507

[13] Maekawa S and Inoue J 1995 *Mater. Sci. Eng.* B **31** 11

[14] Girardeau T, Mimault J, Jaouen M, Chartier P and Tourillon G 1992 *Phys. Rev.* B **46** 7144

[15] JCPDS-ICDD cards 4-783 and 4-850

[16] Profile, Diffrac AT V3.2 Socabim S.A

[17] van Ingen R P, Fastenau R H J and Mittemijer E J 1994 *Phys. Rev. Lett.* **72** 3116
van Ingen R P, Fastenau R H J and Mittemijer E J 1994 *J. Appl. Phys.* **76** 1871
Noyan I C, Huang T C and York B R 1995 *Solid State Mater. Sci.* **20** 125

[18]  van Berkum J G M, Vermeulen A C, Delhez R, de Keijser T H and Mittemeijer E J 1994 *J. Appl. Crystallogr.* **27** 345
      Guinier A 1994 *X-ray Diffraction in Crystals, Imperfect Crystals and Amorphous Bodies* (New York: Dover) p 241
[19]  Mimault J, Faix J J, Girardeau T, Jaouen M and Tourillon G 1994 *Meas. Sci. Technol.* **5** 482
[20]  Gurman S J, Binsted N and Ross I 1984 *J. Phys. C: Solid State Phys.* **17** 143
[21]  Stern E A 1993 *Phys. Rev.* B **48** 9825
[22]  Borowski M 1997 *J. Physique Coll.* IV **7** C2 259
[23]  Apai G, Hamilton J F, Stohr and Thompson A 1979 *Phys. Rev. Lett.* **43** 165
      Balerna A, Bernieri E, Picozzi P, Reale A, Santucci S, Burattini E and Mobilio S 1985 *Phys. Rev.* B **31** 5058
      Montano P A, Shenoy G K, Alp E E, Schulze W and Urban J 1986 *Phys. Rev. Lett.* **56** 2076
[24]  Gladyszewski G 1989 *Thin Solid Films* **170** 99
[25]  Michælsen C 1995 *Phil. Mag.* A **72** 813
[26]  Regnard J R, Manzini I, Revenant C, Rodmacq B and Mimault J, to be published